

# Amorphous AlOCl Compounds Enabling Nanocrystalline LiCl with Abnormally High Ionic Conductivity

Hui Duan,<sup>△</sup> Changhong Wang,<sup>△</sup> Xu-Sheng Zhang, Jiamin Fu, Weihan Li, Jing Wan, Ruizhi Yu, Min Fan, Fucheng Ren, Shuo Wang, Matthew Zheng, Xiaona Li, Jianwen Liang, Rui Wen, Sen Xin, Yu-Guo Guo,\* and Xueliang Sun\*



Cite This: *J. Am. Chem. Soc.* 2024, 146, 29335–29343



Read Online

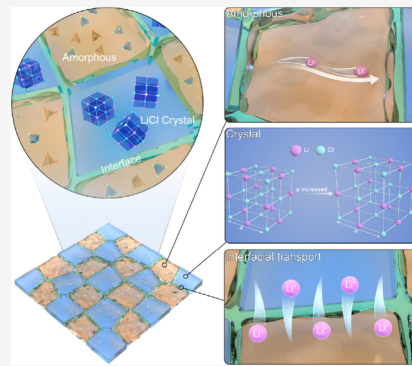
ACCESS |

Metrics & More

Article Recommendations

Supporting Information

**ABSTRACT:** LiCl is a promising solid electrolyte, providing it possesses high ionic conductivity. Numerous efforts have been made to enhance its ionic conductivity through aliovalent doping. However, aliovalent substitution changes the intrinsic structure of LiCl, compromising its cost-effectiveness and electrochemical stability. Here, we report nanocrystalline LiCl embedded in amorphous AlOCl compounds with a heterogeneous structure to enhance its ionic conductivity. Nanocrystallization enlarges the LiCl unit cell, while amorphization facilitates interfacial ion transport. As a result, the amorphous AlOCl-modified LiCl nanocrystal (AlOCl-nanoLiCl) demonstrates a high ionic conductivity of  $1.02 \text{ mS cm}^{-1}$ , which is 5 orders of magnitude higher than that of LiCl. Additionally, it exhibits high oxidative stability, low cost ( $\$19.87 \text{ US kg}^{-1}$ ), and low Young's modulus (2–3 GPa). When AlOCl-nanoLiCl is coupled with Li-rich cathodes ( $\text{Li}_{1.17}\text{Mn}_{0.55}\text{Ni}_{0.24}\text{Co}_{0.05}\text{O}_2$ , 4.8 V vs Li<sup>+</sup>/Li), all-solid-state batteries exhibit remarkable long-term cycling stability (>1000 cycles). This work presents a novel strategy to enhance the ionic conductivity of alkaline chlorides without compromising their intrinsic advantages.



## INTRODUCTION

Solid electrolytes (SEs) have been credited for revolutionizing battery energy density and safety, paving the way for high-voltage all-solid-state lithium metal batteries with practical applications.<sup>1,2</sup> However, SEs face challenges in simultaneously meeting the requirements of superionic conductivity, broad electrochemical stability windows, robust mechanical properties, good air stability, and cost-effectiveness.<sup>3,4</sup> LiCl, as the precursor of many halide SEs, is considered the most promising candidate due to its wide electrochemical stability window, cost-effectiveness, and structural stability.<sup>5</sup> Nevertheless, the direct application of LiCl as a SE is hindered by its extremely low ionic conductivity at room temperature ( $10^{-8} \text{ S cm}^{-1}$  at 25 °C),<sup>6</sup> primarily due to the lack of effective cation transport pathways.

To address this issue, various approaches have been pursued. For instance, substituting monovalent cations in LiCl with aliovalent cations generates cation vacancies via charge compensation, creating lithium-ion transport pathways that facilitate rapid ion diffusion, thus improving the ionic conductivity of LiCl. This strategy resulted in numerous halide SEs, such as  $\text{Li}_3\text{YCl}_6$  ( $0.51 \text{ mS cm}^{-1}$  at 25 °C),<sup>7</sup>  $\text{Li}_3\text{InCl}_6$  ( $1.5 \text{ mS cm}^{-1}$  at 25 °C),<sup>8</sup>  $\text{Li}_3\text{ScCl}_6$  ( $3 \text{ mS cm}^{-1}$  at 25 °C),<sup>9</sup>  $\text{Li}_2\text{Sc}_{2/3}\text{Cl}_4$  ( $1.5 \text{ mS cm}^{-1}$  at 30 °C),<sup>10</sup>  $\text{Li}_2\text{ZrCl}_6$  ( $0.40 \text{ mS cm}^{-1}$  at 30 °C),<sup>11,12</sup> and  $\text{Li}_3\text{YbCl}_6$  ( $0.19 \text{ mS cm}^{-1}$  at 30 °C).<sup>7,8,13–18</sup> However, this aliovalent elemental doping or substitution not only increases the cost and density of LiCl but also changes its

crystal structure, thus greatly compromising its intrinsic merits, such as atom economy, structural stability, and wide electrochemical window.<sup>19</sup> Therefore, it is crucial to explore new strategies for enhancing the ionic conductivity of LiCl without compromising its intrinsic properties.

In this study, distinct from the widely adopted doping or substitution strategy, LiCl nanocrystals are synthesized and embedded in an amorphous AlOCl matrix with a heterogeneous structure, which significantly improves the ionic conductivity of LiCl by 5 orders of magnitude. Systematic structural analyses reveal that nanocrystallization enlarges the unit cell of LiCl, while uniformly dispersing these LiCl nanocrystals in an amorphous AlOCl matrix facilitates interfacial ion transport. As a result, the amorphous AlOCl modified LiCl nanocrystal (AlOCl-nanoLiCl) exhibits a room-temperature ionic conductivity of  $1.02 \text{ mS cm}^{-1}$ , robust oxidative stability, cost-effectiveness ( $\$19.87 \text{ US kg}^{-1}$ ), and low Young's modulus (2–3 GPa). When AlOCl-nanoLiCl is coupled with Li-rich cathodes ( $\text{Li}_{1.17}\text{Mn}_{0.55}\text{Ni}_{0.24}\text{Co}_{0.05}\text{O}_2$ , 4.8 V vs Li<sup>+</sup>/Li), high-voltage all-solid-state batteries demonstrate

Received: May 13, 2024

Revised: October 9, 2024

Accepted: October 10, 2024

Published: October 19, 2024



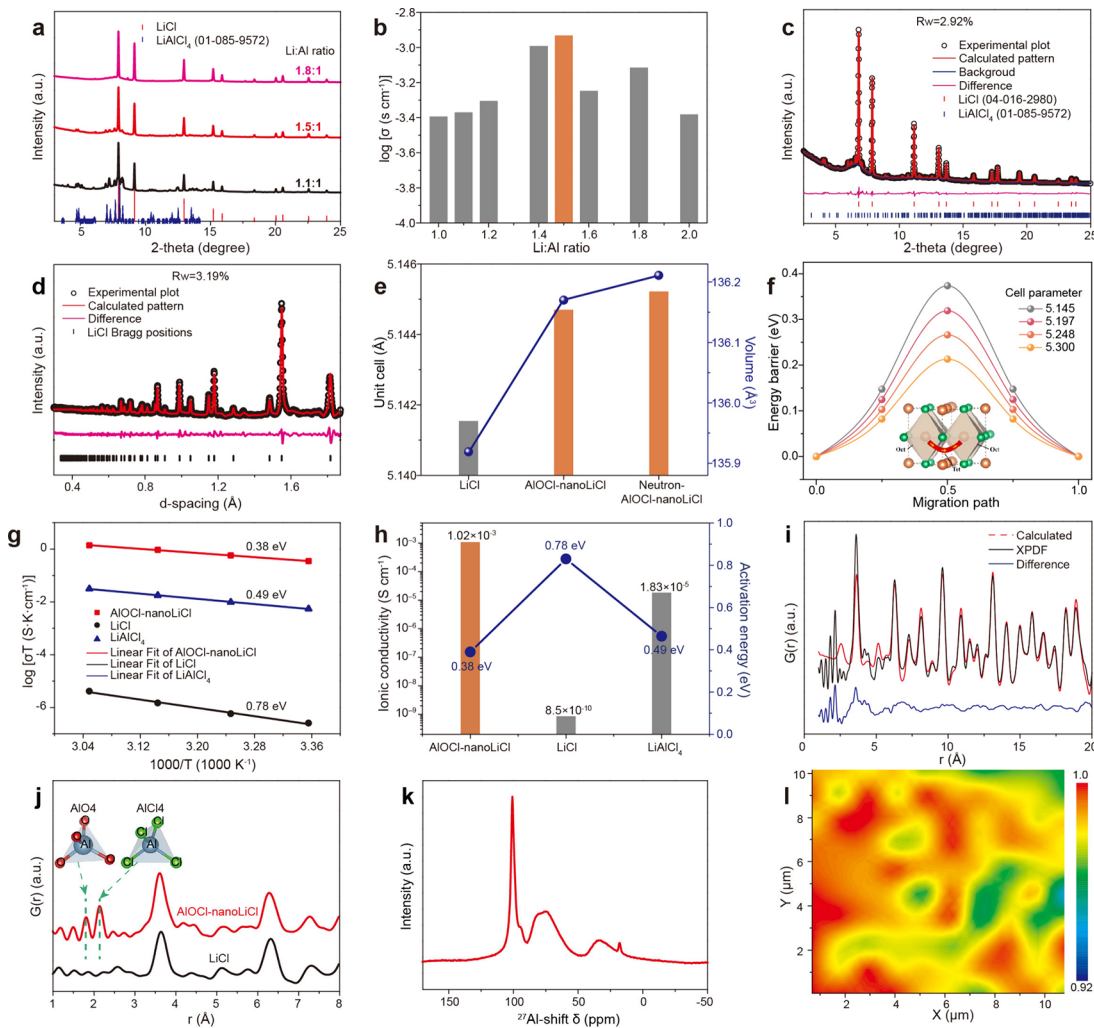


**Figure 1.** Design and characterization of AlOCl-nanoLiCl. (a) Synchrotron-based X-ray diffraction patterns (SXRD,  $\lambda = 0.41027 \text{ \AA}$ ) and (b) ionic conductivities of AlOCl-nanoLiCl with different Li/Al ratios. (c) Rietveld refinement of SXRD ( $\lambda = 0.3542 \text{ \AA}$ ) and (d) neutron diffraction of AlOCl-nanoLiCl. (e) Comparison of the unit cell and volume of AlOCl-nanoLiCl and those of the general LiCl. (f) Comparison of the energy profile of  $\text{Li}^+$  along the migration path from an octahedron site to another in LiCl with different cell parameters. (g) Arrhenius plots and (h) ionic conductivities and activation energies of AlOCl-nanoLiCl, LiCl, and LiAlCl<sub>4</sub> obtained from temperature-dependent EIS measurement. (i) XPDF fitting results of AlOCl-nanoLiCl fitting with LiCl. (j) XPDF profiles of AlOCl-nanoLiCl and LiCl. (k) <sup>27</sup>Al NMR of AlOCl-nanoLiCl. The peak at 20 ppm is spinning sidebands. (l) Raman mapping image of 350 cm<sup>-1</sup> intensity of AlOCl-nanoLiCl (size of the mapped region is  $10 \times 10 \mu\text{m}^2$ ).

exceptional cycling stability (>1000 cycles). This innovative approach has the potential to revolutionize the landscape of all-solid-state battery (ASSB) development, improving both economic feasibility and sustainability.

## RESULTS AND DISCUSSION

**Design and Characterization of AlOCl-nanoLiCl.** The amorphous AlOCl-modified LiCl nanocrystal was synthesized via a one-step, low-temperature annealing process (only 190 °C). Synchrotron X-ray diffraction (SXRD) was conducted to examine the structural features of AlOCl-nanoLiCl with different Li/Al ratios (Figure 1a). With an increasing Li content, the diffraction peaks of LiAlCl<sub>4</sub> weaken, while those of LiCl become more prominent. The ionic conductivities of the AlOCl-nanoLiCl with different Li/Al ratios are shown in Figure 1b and Figure S1. The AlOCl-nanoLiCl with a molar ratio of 1.5:1 was chosen as the optimized electrolyte due to its highest ionic conductivity of  $1.02 \times 10^{-3} \text{ S cm}^{-1}$  at room temperature. The SXRD and neutron diffraction patterns of AlOCl-nanoLiCl closely match the LiCl structure (Figure

1c,d). However, the refinements of SXRD and neutron diffraction indicate that the lattice parameter of AlOCl-modified nanoLiCl is larger than that of typical LiCl (Figure 1e and Table S1). The X-ray-PDF (XPDF) and neutron-PDF (NPDF) were fitted with the structures of LiCl and LiAlCl<sub>4</sub>. The fitting results of XPDF and NPDF all indicate the enlarged unit cell of LiCl (Figure S2 and Table S2), which are consistent with the diffraction refinement results. The larger unit cell results in a larger bottleneck size, causing an increase in ionic conductivity and a decrease in activation energy.<sup>20</sup> DFT calculations were performed to investigate the Li-ion diffusion mechanism in LiCl and the effect of lattice parameter expansion on Li<sup>+</sup> diffusion, as shown in Figure 1f. Li<sup>+</sup> diffusion occurs through ion hopping to the other octahedral sites through an intermediate tetrahedral site. The results show that as the lattice parameters increase from 5.145 to 5.300 Å the diffusion energy barrier gradually decreases from 0.37 to 0.21 eV, indicating that the Li<sup>+</sup> diffusion kinetics can be greatly enhanced with the expansion of battery parameters, which is in good agreement with the experimental results. The corre-

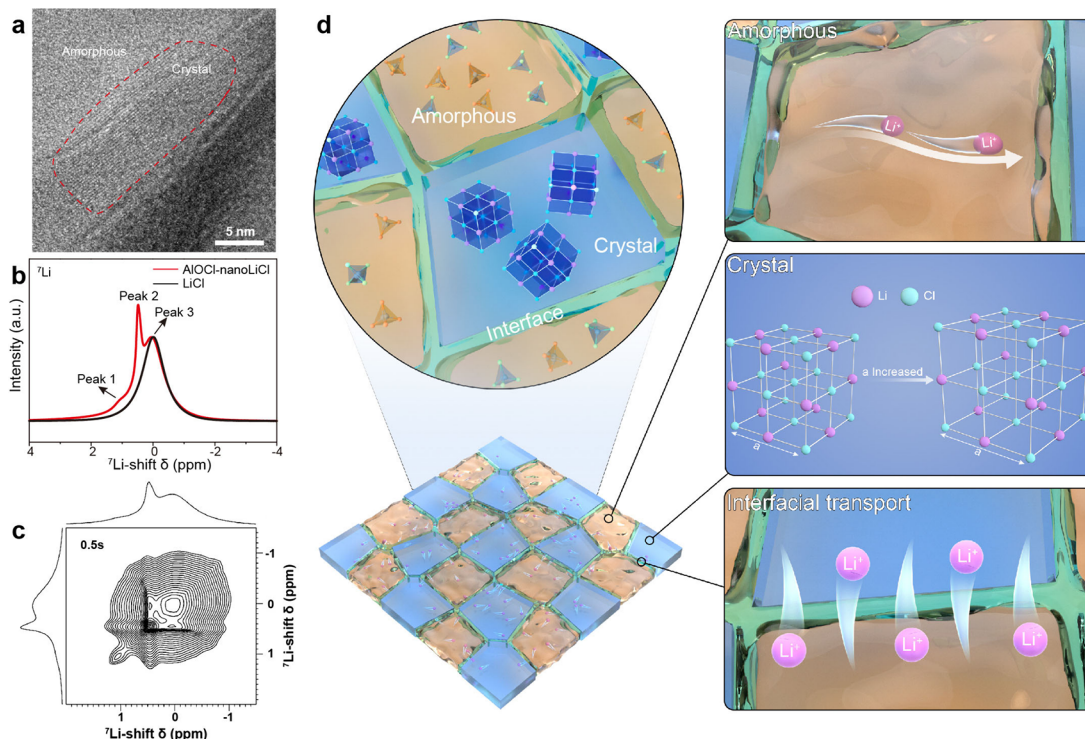


**Figure 2.** Li<sup>+</sup> transport mechanism. (a) High-resolution TEM image of AlOCl-nanoLiCl. (b) 1D <sup>7</sup>Li MAS NMR of AlOCl-nanoLiCl and LiCl. (c) 2D EXSY NMR of AlOCl-nanoLiCl recorded with a mixing time of 0.5 s. (d) Li<sup>+</sup> transport mechanisms in AlOCl-nanoLiCl.

sponding Nyquist plots for AlOCl-nanoLiCl, LiAlCl<sub>4</sub>, and LiCl at different temperatures are presented in Figure S3. The AlOCl-nanoLiCl resistance decreases as the temperature increases. The Arrhenius behavior for the total ion conductivity is plotted in Figure 1g. The activation energy ( $E_a$ ) of AlOCl-nanoLiCl is 0.38 eV, significantly smaller than that of LiCl (0.78 eV) (Figure 1h). Moreover, AlOCl-nanoLiCl exhibits a low electronic conductivity of approximately  $1.2 \times 10^{-9}$  S cm<sup>-1</sup> at room temperature (Figure S4).

The SXRD pattern notably reveals the presence of amorphous phases in AlOCl-nanoLiCl (Figure 1c). A pair distribution function (PDF) analysis was conducted to examine the differences between LiCl and AlOCl-nanoLiCl. In the high-*r* region, AlOCl-nanoLiCl aligned closely with LiCl, suggesting that the primary crystal phase is very similar to that of LiCl (Figure 1i). Significant distinctions are observed in the low-*r* region between AlOCl-nanoLiCl and LiCl (Figure 1j). The peak at 1.796 Å corresponds well with the distance between Al and O in an [AlO<sub>4</sub>]<sup>-</sup> tetrahedron, while the peak at 2.133 Å matches the distance between Al and Cl in the [AlCl<sub>4</sub>]<sup>-</sup> tetrahedron, indicating that the amorphous matrix consists of AlOCl compounds. The composition of AlOCl is AlO<sub>1.32</sub>Cl<sub>0.36</sub>, which was determined by X-ray photoelectron spectroscopy (XPS) analysis (Figure S5 and Table S3).

Furthermore, nuclear magnetic resonance (NMR) is utilized to analyze the chemical environment of the Al nuclei. The <sup>27</sup>Al NMR spectrum of AlOCl-nanoLiCl displays peaks at 100.68, 80.79, and 32.41 ppm (Figure 1k). The sharp peak at 100.68 ppm corresponds to [AlCl<sub>4</sub>]<sup>-</sup> tetrahedra,<sup>21</sup> while the broad peak at 80.79 ppm corresponds to tetrahedrally coordinated [AlCl<sub>4-x</sub>O<sub>x</sub>]<sup>-</sup> (1 ≤ *x* ≤ 4) species.<sup>22,23</sup> Additionally, the peak at 32.41 ppm corresponds to highly distorted [AlO<sub>4</sub>]<sup>-</sup> or unsaturated penta-coordinated Al ions [AlO<sub>5</sub>]<sup>-</sup>,<sup>24-26</sup> exclusively found in the amorphous phase and not in any of the

related crystal phases.<sup>23</sup> The asymmetric broadening of the NMR signal associated with [AlCl<sub>4-x</sub>O<sub>x</sub>]<sup>-</sup>, [AlO<sub>4</sub>]<sup>-</sup>, and [AlO<sub>5</sub>]<sup>-</sup> shows a tail toward low chemical shift values due to local structural disorder, resulting in a distribution of chemical shift values.<sup>27</sup>

Further confirmation of the structural features of the amorphous AlOCl compounds was obtained through X-ray absorption spectroscopy and Raman analyses. After comparing the Cl X-ray absorption near-edge structure (XANES) spectra of the AlOCl-nanoLiCl compounds with reference spectra from AlCl<sub>3</sub> and LiCl, it is evident that the AlOCl-nanoLiCl compounds present mixed features of both AlCl<sub>3</sub> and LiCl. Specifically, they display three white line peaks at 2826.0, 2827.06, and 2828.74 eV, along with a pre-edge feature at 2821.2 eV (Figure S6). This suggests that the local environment surrounding Cl in the AlOCl-nanoLiCl compounds comprises a combination of local structures similar to those found in AlCl<sub>3</sub> and LiCl. Additionally, the Raman spectra of AlOCl-nanoLiCl exhibit the vibrational peak of the [AlCl<sub>4</sub>]<sup>-</sup> tetrahedron at 350 cm<sup>-1</sup> (Figure S7), indicating the uniform distribution of [AlCl<sub>4</sub>]<sup>-</sup> in the whole material (Figure 1l and S8). These structural analyses consistently suggest that the amorphous AlOCl matrix consists of [AlCl<sub>4-x</sub>O<sub>x</sub>]<sup>-</sup>, [AlO<sub>4</sub>]<sup>-</sup>, and [AlCl<sub>4</sub>]<sup>-</sup> tetrahedra as well as [AlO<sub>5</sub>]<sup>-</sup> hexahedra.

Transmission electron microscopy (TEM) was employed to examine the microstructure of the AlOCl-nanoLiCl electrolyte. As shown in Figure 2a, TEM images demonstrate the coexistence of crystalline and amorphous phases. The particle size of LiCl nanocrystals is about 5–20 nm (Figure S9). The (200) interplanar spacing of AlOCl-nanoLiCl is found to be 2.59 Å, which is consistent with the XRD results (Figure S10a). Additionally, TEM energy-dispersive X-ray spectra (EDS) mapping and scanning electron microscopy (SEM) EDS of AlOCl-nanoLiCl indicate a uniform dispersion of the

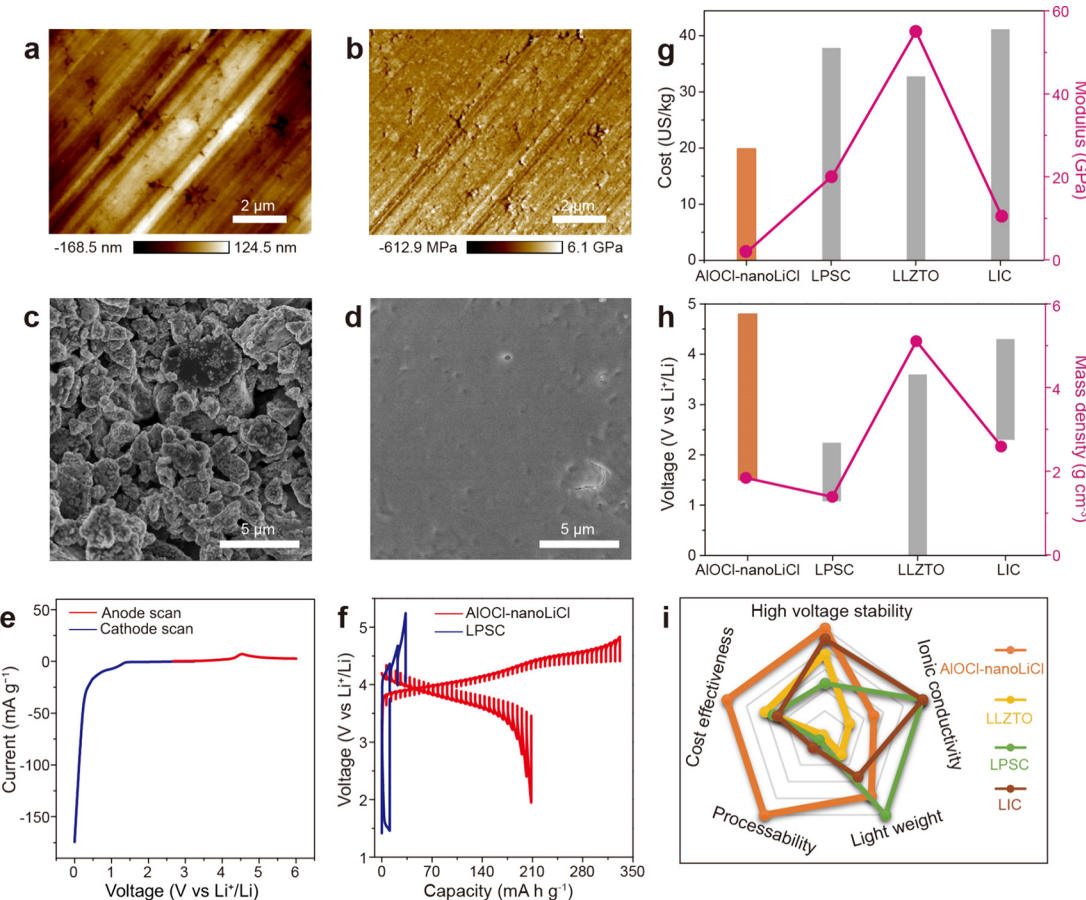


**Figure 3.** Mechanical properties and electrochemical stability. (a, b) AFM topography images and Young's modulus distribution of AlOCl-nanoLiCl pellets. Cross-section SEM images of (c) LPSC and (d) AlOCl-nanoLiCl solid electrolyte cold-pressed at 125 MPa pressure. (e) Anode scan and cathode scan of the all-solid-state Li/LPSC/AlOCl-nanoLiCl/AlOCl-nanoLiCl@C battery at 0.1 mV s<sup>-1</sup>. (f) GITT of all-solid-state Li-In/LPSC/AlOCl-nanoLiCl/LLO and Li-In/LPSC/LLO batteries. (g) Cost and modulus, (h) electrochemical stability window and mass density, and (i) comprehensive comparison of AlOCl-nanoLiCl with various solid electrolytes. The solid electrolytes include oxides ( $\text{Li}_{6.5}\text{La}_3\text{Zr}_{1.5}\text{Ta}_{0.5}\text{O}_{12}$  (LLZTO)<sup>33–35</sup>), sulfides ( $\text{Li}_6\text{PS}_3\text{Cl}$  (LPSC)<sup>36–38</sup>) and halides ( $\text{Li}_3\text{InCl}_6$  (LIC)<sup>8,39</sup>).

constituent elements, including Al, O, and Cl (Figure S10b and S11). Moreover, linear scanning in the crystal region with TEM demonstrates consistent variations in the Al, O, and Cl elements (Figure S12). This heterogeneous structure, where nanoLiCl is embedded in AlOCl compounds, is expected to enhance ion transport at both bulk and interface levels due to the nanoscale effect and interface engineering.<sup>28–30</sup>

One-dimensional (1D) <sup>7</sup>Li magic angle spinning (MAS) was conducted to analyze the Li chemical environment in the electrolytes (Figure 2b). External solid crystal LiCl was used as a chemical shift reference ( $\delta = 0.00$  ppm). The <sup>7</sup>Li MAS NMR spectra of AlOCl-nanoLiCl exhibited three peaks localized at 0.03 ppm (peak 3), 0.47 ppm (narrow peak, peak 2), and 1.04 ppm (broad peak, peak 1), indicating different chemical environments of lithium. The full width at half-maximum (FWHM) of peaks 1, 2, and 3 were 0.74, 0.21, and 1, respectively. The position and FWHM of peak 3 were similar to those of LiCl suggesting the origin of the peak at 0.03 ppm from the octahedrally coordinated  $\text{LiCl}_6$  site in the AlOCl-nanoLiCl. The peak at 0.47 ppm corresponds to the  $\text{LiCl}_6$  6-fold coordinated Li octahedron in the amorphous phase, which shifts to higher values due to local structural disorder.<sup>24</sup> The shoulder peak at 1.04 ppm represents Li at the amorphous/crystal interface.<sup>31</sup> Additionally, the FWHM of peak 2 is significantly lower than that of peaks 3 and 1, indicating fast

$\text{Li}^+$  transport dynamics.<sup>32</sup> The area ratio of peak 3/peak 2/peak 1 was 0.78:0.16:0.06, indicating a low content of peak 2. The slightly higher chemical shift of peak 3 (0.03 ppm) in AlOCl-nanoLiCl compared to pure LiCl (0.00 ppm) suggests reduced interaction between  $\text{Li}^+$  cations and  $\text{Cl}^-$  anions in the  $\text{LiCl}_6$  octahedron of AlOCl-nanoLiCl compared to crystalline LiCl, consistent with SXRD refinement results indicating an increased unit cell size in AlOCl-nanoLiCl. Therefore, both the crystalline and the amorphous phases play crucial roles in Li-ion transport.

Considering that two-dimensional <sup>7</sup>Li–<sup>7</sup>Li exchange spectroscopy (2D EXSY) is capable of measuring spontaneous  $\text{Li}^+$  exchange between different  $\text{Li}^+$  environments, 2D EXSY was conducted to elucidate the underlying mechanism of the  $\text{Li}^+$  transport in the AlOCl-nanoLiCl electrolyte. At a mixing time of 0.5 s, distinct peaks appeared on the diagonal, indicating  $\text{Li}^+$  transport within the same component (Figure 2c). Furthermore, off-diagonal peaks can be observed among the three signals, indicating  $\text{Li}^+$  diffusion between different  $\text{Li}^+$  environments. These findings suggest rapid  $\text{Li}^+$  exchange within these three Li chemical environments and at the interface, particularly along and between enlarged LiCl nanocrystals and amorphous AlOCl compounds.

Based on the above structural and Li-ion dynamics analyses, the factors contributing to the rapid  $\text{Li}^+$  transport mechanism

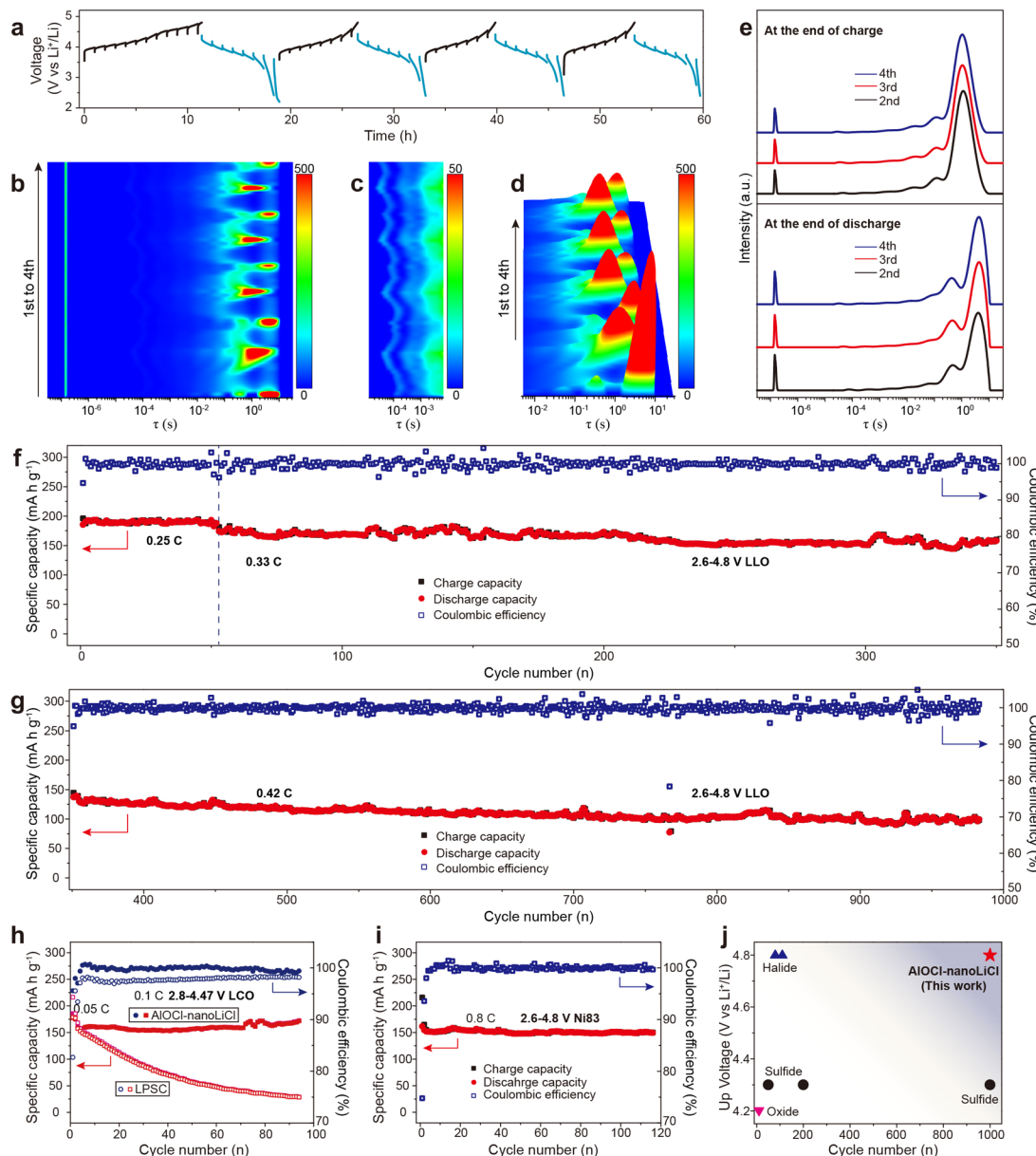


**Figure 4.** Electrochemical performance of AlOCl-nanoLiCl-based ASSBs. (a–e) Li-In/LPSC/AlOCl-nanoLiCl/LLO battery impedance spectra evolution during galvanostatic battery cycling at a current density of  $0.09 \text{ mA cm}^{-2}$  between 2.6 and 4.8 V vs  $\text{Li}^+/\text{Li}$ . (a) Initial four cycles of charge and discharge voltage profile showing current interruption corresponding to the periods of impedance measurement. (b–d) DRT results during charge and discharge periods of the initial four cycles. (e) Comparison of the DRT results at the end of charge (top) and discharge (bottom) from the 2nd cycle to the 4th cycle. (f–i) Long-term cycling stability and Coulombic efficiency of all-solid-state (f, g) Li-In/LPSC/AlOCl-nanoLiCl/LLO battery between 2.6 and 4.8 V after in situ EIS measurement, (h) Li-In/LPSC/AlOCl-nanoLiCl/4.47LCO battery and Li-In/LPSC/4.47LCO battery between 2.8 and 4.47 V, and (i) Li-In/LPSC/AlOCl-nanoLiCl/Ni83 battery between 2.6 and 4.8 V vs  $\text{Li}^+/\text{Li}$  at room temperature. (j) Electrochemical performance comparison of Li-based SEs with bare cathodes.<sup>43–48</sup>

are outlined below. First, the enlarged unit cell of LiCl results in a larger bottleneck size, enhancing the speed of  $\text{Li}^+$  transport. Second, the amorphous phase may exhibit high ionic conductivity. Third, the interface between the amorphous AlOCl and LiCl nanocrystals provides a rapid  $\text{Li}^+$  transport pathway (Figure 2d).

#### Mechanical Properties and Electrochemical Stability.

The mechanical properties of SEs also have a crucial role in their application in all-solid-state batteries.<sup>40</sup> Atomic force microscopy (AFM) was carried out to quantitatively determine the Young's modulus of AlOCl-nanoLiCl. AFM topography and mechanical analysis revealed that the AlOCl-nanoLiCl has

a low average Young's modulus of 2–3 GPa (Figure 3a,b), which is comparable to that of the polymer electrolytes and significantly lower than that of the softest inorganic ionic conductor sulfide SEs (20 GPa) (Figure 3g).<sup>41</sup> This favorable deformability leads to a tight and compatible contact between AlOCl-nanoLiCl particles without a grain boundary under a low pressure of 125 MPa. In contrast, the  $\text{Li}_6\text{PS}_5\text{Cl}$  (LPSC) pellet exhibits an obvious porous structure (Figure 3c,d). Compared to high-temperature ( $>1000^\circ\text{C}$ ) sintering processes of oxide SEs and cold-pressing or hot-pressing processes of sulfide SEs, AlOCl-nanoLiCl is more favorable for low-pressure fabrication processes and more feasible for

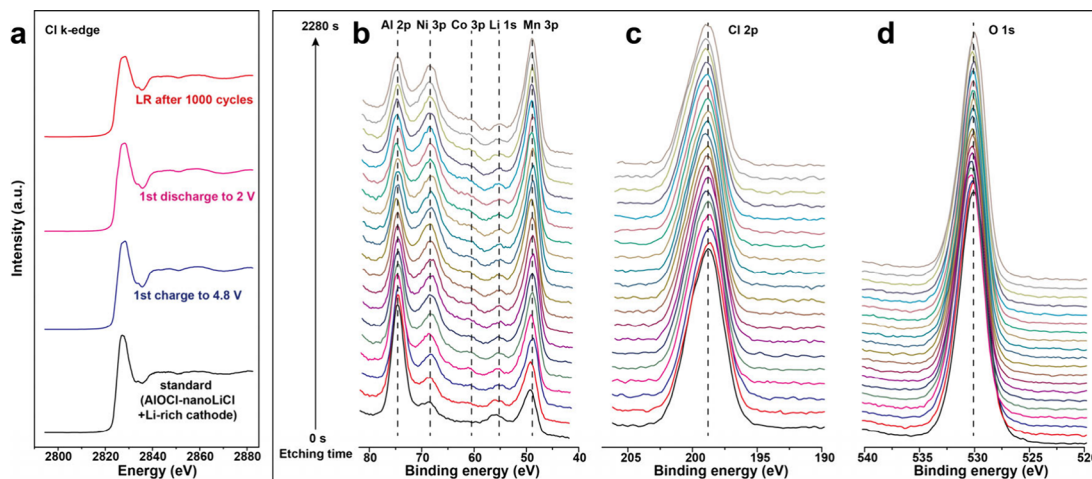


**Figure 5.** Electrochemical stability of AlOCl-nanoLiCl in Li-In/LPSC/AlOCl-nanoLiCl/LLO cathode battery during the charge/discharge process and after 1000 cycles. (a) Ex situ Cl K-edge XANES spectra of AlOCl-nanoLiCl-LLO cathode composites at different states. XPS depth profile of (b) Al 2p, Ni 3p, Co 3p, Li 1s, Mn 3p, (c) Cl 2p, and (d) O 1s XPS of the cathode composites in Li-In/LPSC/AlOCl-nanoLiCl/LLO cathode battery after 1000 cycles.

achieving large-scale and thin SE membranes, compatible with commercial roll-to-roll fabrication processes.

Apart from soft mechanical properties, electrochemical stability is also important for realizing high-performance ASSBs. In the linear sweep voltammetry (LSV) test, the LPSC electrolyte is used as an interlayer between AlOCl-nanoLiCl and the Li metal. Anodic scanning reveals only a small peak around 4.5 V (Figure 3e), which is attributed to the oxidation of M–Cl bonds.<sup>17</sup> No further decomposition was observed in the second cycle (Figure S13), indicating the formation of a stable cathode–electrolyte interphase in the initial process. Additionally, no discernible side products are detected in AlOCl-nanoLiCl by XRD after anodic scanning (Figure S14), suggesting good electrochemical oxidation stability. Thus, this electrolyte may be compatible with high-voltage cathodes. No significant reduction peak is observed in the cathode scanning. The current shows a weak increase below 1.4 V but significantly increases below 0.5 V. To further assess the intrinsic compatibility between high-voltage cathode and AlOCl-nanoLiCl electrolyte, bare Li-rich layered oxide (LLO) cathodes ( $\text{Li}_{1.17}\text{Mn}_{0.55}\text{Ni}_{0.24}\text{Co}_{0.05}\text{O}_2$ ) without any coating or modification were used to assemble Li-In/LPSC/AlOCl-nanoLiCl/LLO batteries. EIS measurements over time yield almost identical spectra after 18 h (Figure S15), corroborating the good chemical stability of the LLO cathode in direct contact with AlOCl-nanoLiCl. The galvanostatic intermittent titration technique (GITT) was employed to evaluate the thermodynamic compatibility between bare LLO cathodes and AlOCl-nanoLiCl and to mitigate the dynamic impact of oxidation in the cathode composite during the electrochemical process. Compared to LPSC-based batteries, AlOCl-nanoLiCl-based batteries exhibited high Coulombic efficiency, with no side reactions occurring at high voltage over sufficient reaction time (Figure 3f), indicating the high stability of AlOCl-nanoLiCl toward LLO cathodes. These findings underscore the suitability of AlOCl-nanoLiCl as a high-voltage SE with excellent compatibility with a bare high-voltage cathode (Figure 3h).

The cost of SEs is also crucial for their practical application, which includes the raw material price and preparation cost. The AlOCl-nanoLiCl developed here has a low raw material

cost because of the high abundance of Al and O elements<sup>42</sup> (Figure S16) and low preparation cost resulting from the one-step low-temperature synthesis (only 190 °C). If a solid-state electrolyte is produced on a large scale, then the cost of raw materials can closely align with the elemental costs. Thus, the overall price can be estimated by considering the proportion of each element used in the synthesis. The calculated price of AlOCl-nanoLiCl is \$19.87 US kg<sup>-1</sup>, which is significantly lower than that of the reported inorganic SEs (Figure 3g). Furthermore, compared to other rare-earth-metal-based halides and oxides, AlOCl-nanoLiCl possesses a lower density of 1.82 g cm<sup>-3</sup>, which is beneficial for obtaining high energy density in ASSBs (Figure 3h). Taking all of the discussion into account, AlOCl-nanoLiCl emerges as an ideal solid electrolyte, combining at least five advantages: high ionic conductivity, low cost, wide electrochemical window, good deformability, and lightweight (Figure 3i).

**Electrochemical Performance of All-Solid-State Batteries.** To fulfill the advantages of AlOCl-nanoLiCl, a bare  $\text{Li}_{1.17}\text{Mn}_{0.55}\text{Ni}_{0.24}\text{Co}_{0.05}\text{O}_2$  (LLO) cathode was chosen to fabricate high-energy-density and high-voltage ASSBs with a configuration of Li-In/LPSC/AlOCl-nanoLiCl/LLO. To assess interface stability, in situ EIS in combination with distribution of relaxation time (DRT) analysis was conducted during the initial charge and discharge processes.<sup>49</sup> The evolution of the impedance spectra with the open circuit voltage (OCV) is shown in Figure S17, revealing changes dependent on the battery state-of-charge (SOC), especially in the lower frequency range. The middle- and low-frequency regions include many complex processes, such as the resistance of lithium ions through the surface film and the charge transfer impedance occurring in the cathode and anode. As shown in Figures 4b–e and S18, the SOC-dependent DRT analysis of the full battery revealed that these regions mainly comprise four processes. First,  $\tau_1$  at about 10<sup>-7</sup> s corresponds to the bulk resistance of AlOCl-nanoLiCl, which remains stable with SOC growth during the initial four cycles. Second, a peak at  $\tau_2$  occurs in the time constant of 10<sup>-4</sup> s, corresponding to the solid electrolyte interphase (SEI) variation with the SOC due to the lithiation and delithiation. The intensity of  $\tau_2$  is very weak and shows insignificant change from the 1st to the 4th

cycle (Figure 4c), indicating stable and fast  $\text{Li}^+$  transport in the SEI. Third, two peaks,  $\tau_3$  (0.1 to 1 s) and  $\tau_4$  (1 to 10 s), corresponding to charge transfer resistance ( $R_{ct}$ ), change significantly with SOC.<sup>48</sup> Both  $\tau_3$  and  $\tau_4$  are electrochemically reversible during cycling (Figure 4d), and their time constant and intensity were well maintained at the same SOC after the initial activation process (Figure 4e). Such stable impedance at the same SOC confirms stable charge transfer kinetics and electrode/electrolyte interface and high oxidation stability of AlOCl-nanoLiCl (up to 4.8 V vs  $\text{Li}^+/\text{Li}$ ), which guarantees the electrochemical performance of high-voltage ASSBs.

The Li-In/LPSC/AlOCl-nanoLiCl/LLO battery possesses a discharge capacity exceeding 210 mA h g<sup>-1</sup> with a voltage plateau at 4.5 V (Figure 4a and S19). After about 1000 cycles at different current densities, the battery demonstrated high-capacity retention of 75% with high average Coulombic efficiency of 99.8% (Figure 4f,g). For comparison, the Li-In/LPSC/LLO solid battery shows a much lower reversible capacity and poor cycling performance with a low Coulombic efficiency of less than 80% (Figure S20). Apart from high-voltage and high-capacity Li-rich cathodes, other high-voltage cathodes, such as 4.47 V  $\text{LiCoO}_2$  and single crystal  $\text{LiNi}_{0.83}\text{Mn}_{0.07}\text{Co}_{0.1}\text{O}_2$  (Ni83, 2.6–4.8 V), were also selected to demonstrate high-voltage ASSBs and also demonstrated excellent electrochemical cycling stability (Figures 4h,i and S21, S22, and S23). These results indicate the superior high-voltage cathode compatibility of AlOCl-nanoLiCl (Figure 4j).

To investigate the chemical stability between LLO and AlOCl-nanoLiCl after electrochemical cycling, X-ray absorption spectroscopy and XPS analyses were performed. Cl K-edge XANES spectra of the samples at different charge/discharge states and the sample after 1000 cycles showed no obvious change, demonstrating the electrochemical stability of AlOCl-nanoLiCl toward high-voltage LLO (Figure 5a). Moreover, XPS depth sputtering was carried out to detect variation of the composite cathode after 1000 cycles. The peak positions of Al 2p, Ni 3p, Co 3p, Li 1s, Mn 3p, Cl 2p, and O 1s remained unchanged with different etching depths. No new products were found on the surface or inside of the cathode (Figure 5b–d) after cycling, further confirming the electrochemical stability of AlOCl-nanoLiCl with high-voltage LLO cathodes.

## CONCLUSIONS

In this work, we have innovatively synthesized amorphous AlOCl compounds modified LiCl nanocrystals (AlOCl-nano-LiCl), which exhibit abnormally high ionic conductivity of  $1.02 \times 10^{-3}$  S cm<sup>-1</sup> at room temperature. Such high room-temperature ionic conductivity originated from the rapid ion transport within the amorphous phase, at the interface region, and within the nanocrystalline LiCl with enlarged unit cells. In addition, the AlOCl-nanoLiCl exhibited exceptional deformability, characterized by a low Young's modulus of 2–3 GPa and has a low cost of \$19.87 US kg<sup>-1</sup>. Importantly, this solid electrolyte possesses an extremely wide electrochemical window and excellent chemical/electrochemical stability, particularly toward high-voltage cathodes. High-voltage all-solid-state batteries (ASSBs) incorporating AlOCl-nanoLiCl electrolytes and high-voltage Li-rich cathodes (2–4.8 V vs  $\text{Li}^+/\text{Li}$ ) demonstrated outstanding electrochemical performance. These electrolytes are not only cost-effective and recyclable but also nontoxic and ductile, making them promising candidates for next-generation energy storage applications.

## ASSOCIATED CONTENT

### Supporting Information

The Supporting Information is available free of charge at <https://pubs.acs.org/doi/10.1021/jacs.4c06498>.

Experimental methods; additional electrochemical performance; EDS mapping results; EIS and DRT results, supplemental figures and tables (PDF)

## AUTHOR INFORMATION

### Corresponding Authors

**Yu-Guo Guo** – CAS Key Laboratory of Molecular Nanostructure and Nanotechnology, CAS Research/Education Center for Excellence in Molecular Sciences, Institute of Chemistry, Chinese Academy of Sciences (CAS), Beijing 100190, P. R. China;  [orcid.org/0000-0003-0322-8476](https://orcid.org/0000-0003-0322-8476); Email: [yguo@iccas.ac.cn](mailto:yguo@iccas.ac.cn)

**Xueliang Sun** – Department of Mechanical and Materials Engineering, University of Western Ontario, London, Ontario N6A 5B9, Canada; Ningbo Key Laboratory of All-Solid-State Battery, Eastern Institute for Advanced Study, Eastern Institute of Technology, Ningbo, Zhejiang 315200, P.R. China;  [orcid.org/0000-0003-0374-1245](https://orcid.org/0000-0003-0374-1245); Email: [xsun9@uwo.ca](mailto:xsun9@uwo.ca)

### Authors

**Hui Duan** – Department of Mechanical and Materials Engineering, University of Western Ontario, London, Ontario N6A 5B9, Canada; Engineering Research Center of the Ministry of Education for Advanced Battery Materials, Hunan Provincial Key Laboratory of Nonferrous Value-Added Metallurgy, School of Metallurgy and Environment, Central South University, Changsha 410083, P. R. China

**Changhong Wang** – Ningbo Key Laboratory of All-Solid-State Battery, Eastern Institute for Advanced Study, Eastern Institute of Technology, Ningbo, Zhejiang 315200, P.R. China;  [orcid.org/0000-0002-4201-0130](https://orcid.org/0000-0002-4201-0130)

**Xu-Sheng Zhang** – CAS Key Laboratory of Molecular Nanostructure and Nanotechnology, CAS Research/Education Center for Excellence in Molecular Sciences, Institute of Chemistry, Chinese Academy of Sciences (CAS), Beijing 100190, P. R. China;  [orcid.org/0000-0002-3039-9222](https://orcid.org/0000-0002-3039-9222)

**Jiamin Fu** – Department of Mechanical and Materials Engineering, University of Western Ontario, London, Ontario N6A 5B9, Canada

**Weihai Li** – Department of Mechanical and Materials Engineering, University of Western Ontario, London, Ontario N6A 5B9, Canada

**Jing Wan** – CAS Key Laboratory of Molecular Nanostructure and Nanotechnology, CAS Research/Education Center for Excellence in Molecular Sciences, Institute of Chemistry, Chinese Academy of Sciences (CAS), Beijing 100190, P. R. China

**Ruiwei Yu** – Department of Mechanical and Materials Engineering, University of Western Ontario, London, Ontario N6A 5B9, Canada

**Min Fan** – CAS Key Laboratory of Molecular Nanostructure and Nanotechnology, CAS Research/Education Center for Excellence in Molecular Sciences, Institute of Chemistry, Chinese Academy of Sciences (CAS), Beijing 100190, P. R. China

Fucheng Ren — Ningbo Key Laboratory of All-Solid-State Battery, Eastern Institute for Advanced Study, Eastern Institute of Technology, Ningbo, Zhejiang 315200, P.R. China; [ORCID iD](https://orcid.org/0000-0001-7078-6238)

Shuo Wang — Ningbo Key Laboratory of All-Solid-State Battery, Eastern Institute for Advanced Study, Eastern Institute of Technology, Ningbo, Zhejiang 315200, P.R. China; [ORCID iD](https://orcid.org/0000-0002-7907-9676)

Matthew Zheng — Department of Mechanical and Materials Engineering, University of Western Ontario, London, Ontario N6A 5B9, Canada

Xiaona Li — Ningbo Key Laboratory of All-Solid-State Battery, Eastern Institute for Advanced Study, Eastern Institute of Technology, Ningbo, Zhejiang 315200, P.R. China; [ORCID iD](https://orcid.org/0000-0001-6713-2997)

Jianwen Liang — Department of Mechanical and Materials Engineering, University of Western Ontario, London, Ontario N6A 5B9, Canada; [ORCID iD](https://orcid.org/0000-0003-4055-1301)

Rui Wen — CAS Key Laboratory of Molecular Nanostructure and Nanotechnology, CAS Research/Education Center for Excellence in Molecular Sciences, Institute of Chemistry, Chinese Academy of Sciences (CAS), Beijing 100190, P. R. China; [ORCID iD](https://orcid.org/0000-0003-2644-7452)

Sen Xin — CAS Key Laboratory of Molecular Nanostructure and Nanotechnology, CAS Research/Education Center for Excellence in Molecular Sciences, Institute of Chemistry, Chinese Academy of Sciences (CAS), Beijing 100190, P. R. China; [ORCID iD](https://orcid.org/0000-0002-0546-0626)

Complete contact information is available at:

<https://pubs.acs.org/10.1021/jacs.4c06498>

## Author Contributions

▽ H.D. and C.W. contributed equally to this work. The manuscript was written through the contributions of all authors. All authors have approved the final version of the manuscript.

## Notes

The authors declare no competing financial interest.

## ACKNOWLEDGMENTS

This work was supported by the Natural Sciences and Engineering Research Council of Canada (NSERC), Canada Research Chair Program (CRC), Canada Foundation for Innovation (CFI), Ontario Research Fund (ORF), China Automotive Battery Research Institute Co., Ltd., Glabat Solid-State Battery Inc., University of Western Ontario, and the CAS Project for Young Scientists in Basic Research (Grant No. YSBR-058). H.D. and R.Y. appreciate the support of Mitacs through the Mitacs Accelerate program. We acknowledge Ningning Wu at the Center for Physicochemical Analysis and Measurements in ICCAS for the NMR measurements and analysis. We thank the High-Performance Computing Platform at the Eastern Institute of Technology (Ningbo) for its computational resources.

## REFERENCES

- (1) Janek, J.; Zeier, W. G. A Solid Future for Battery Development. *Nat. Energy* **2016**, *1*, 16141.
- (2) Manthiram, A.; Yu, X.; Wang, S. Lithium battery chemistries enabled by solid-state electrolytes. *Nature Rev. Mater.* **2017**, *2*, 16103.
- (3) Famprikis, T.; Canepa, P.; Dawson, J. A.; Islam, M. S.; Masquelier, C. Fundamentals of inorganic solid-state electrolytes for batteries. *Nat. Mater.* **2019**, *18*, 1278.
- (4) Chen, R.; Li, Q.; Yu, X.; Chen, L.; Li, H. Approaching Practically Accessible Solid-State Batteries: Stability Issues Related to Solid Electrolytes and Interfaces. *Chem. Rev.* **2020**, *120*, 6820.
- (5) Zhu, Y.; He, X.; Mo, Y. Origin of Outstanding Stability in the Lithium Solid Electrolyte Materials: Insights from Thermodynamic Analyses Based on First-Principles Calculations. *ACS Appl. Mater. Interfaces* **2015**, *7*, 23685.
- (6) Court-Castagnet, R.; Kaps, C.; Cros, C.; Hagenmuller, P. Ionic conductivity-enhancement of LiCl by homogeneous and heterogeneous dopings. *Solid State Ionics* **1993**, *61*, 327.
- (7) Asano, T.; Sakai, A.; Ouchi, S.; Sakaida, M.; Miyazaki, A.; Hasegawa, S. Solid Halide Electrolytes with High Lithium-Ion Conductivity for Application in 4 V Class Bulk-Type All-Solid-State Batteries. *Adv. Mater.* **2018**, *30*, 1803075.
- (8) Li, X.; Liang, J.; Luo, J.; Norouzi Banis, M.; Wang, C.; Li, W.; Deng, S.; Yu, C.; Zhao, F.; Hu, Y.; Sham, T.-K.; Zhang, L.; Zhao, S.; Lu, S.; Huang, H.; Li, R.; Adair, K. R.; Sun, X. Air-stable  $\text{Li}_3\text{InCl}_6$  electrolyte with high voltage compatibility for all-solid-state batteries. *Energy Environ. Sci.* **2019**, *12*, 2665.
- (9) Liang, J.; Li, X.; Wang, S.; Adair, K. R.; Li, W.; Zhao, Y.; Wang, C.; Hu, Y.; Zhang, L.; Zhao, S.; Lu, S.; Huang, H.; Li, R.; Mo, Y.; Sun, X. Site-Occupation-Tuned Superionic  $\text{Li}_x\text{ScCl}_{3+x}$  Halide Solid Electrolytes for All-Solid-State Batteries. *J. Am. Chem. Soc.* **2020**, *142*, 7012.
- (10) Zhou, L.; Kwok, C. Y.; Shyamsunder, A.; Zhang, Q.; Wu, X.; Nazar, L. F. A new halospinel superionic conductor for high-voltage all solid state lithium batteries. *Energy Environ. Sci.* **2020**, *13*, 2056.
- (11) Kwak, H.; Han, D.; Lyoo, J.; Park, J.; Jung, S. H.; Han, Y.; Kwon, G.; Kim, H.; Hong, S.-T.; Nam, K.-W.; Jung, Y. S. New Cost-Effective Halide Solid Electrolytes for All-Solid-State Batteries: Mechanically Prepared  $\text{Fe}^{3+}$ -Substituted  $\text{Li}_2\text{ZrCl}_6$ . *Adv. Energy Mater.* **2021**, *11*, 2003190.
- (12) Wang, K.; Ren, Q.; Gu, Z.; Duan, C.; Wang, J.; Zhu, F.; Fu, Y.; Hao, J.; Zhu, J.; He, L.; Wang, C.-W.; Lu, Y.; Ma, J.; Ma, C. A cost-effective and humidity-tolerant chloride solid electrolyte for lithium batteries. *Nat. Commun.* **2021**, *12*, 4410.
- (13) Park, J.; Han, D.; Kwak, H.; Han, Y.; Choi, Y. J.; Nam, K.-W.; Jung, Y. S. Heat treatment protocol for modulating ionic conductivity via structural evolution of  $\text{Li}_{3-x}\text{Yb}_{1-x}\text{M}_x\text{Cl}_6$  ( $\text{M} = \text{Hf}^{4+}, \text{Zr}^{4+}$ ) new halide superionic conductors for all-solid-state batteries. *Chem. Eng. J.* **2021**, *425*, 130630.
- (14) Hu, J.; Yao, Z.; Chen, K.; Li, C. High-conductivity open framework fluorinated electrolyte bonded by solidified ionic liquid wires for solid-state Li metal batteries. *Energy Storage Mater.* **2020**, *28*, 37.
- (15) Schlem, R.; Muy, S.; Prinz, N.; Banik, A.; Shao-Horn, Y.; Zobel, M.; Zeier, W. G. Mechanochemical Synthesis: A Tool to Tune Cation Site Disorder and Ionic Transport Properties of  $\text{Li}_3\text{MCl}_6$  ( $\text{M} = \text{Y}, \text{Er}$ ) Superionic Conductors. *Adv. Energy Mater.* **2020**, *10*, 1903719.
- (16) Park, K.-H.; Kaup, K.; Assoud, A.; Zhang, Q.; Wu, X.; Nazar, L. F. High-Voltage Superionic Halide Solid Electrolytes for All-Solid-State Li-Ion Batteries. *ACS Energy Lett.* **2020**, *5*, 533.
- (17) Liang, J.; Li, X.; Adair, K. R.; Sun, X. Metal Halide Superionic Conductors for All-Solid-State Batteries. *Acc. Chem. Res.* **2021**, *54*, 1023.
- (18) Muy, S.; Voss, J.; Schlem, R.; Koerver, R.; Sedlmaier, S. J.; Maglia, F.; Lamp, P.; Zeier, W. G.; Shao-Horn, Y. High-Throughput Screening of Solid-State Li-Ion Conductors Using Lattice-Dynamics Descriptors. *Iscience* **2019**, *16*, 270.
- (19) Wang, S.; Bai, Q.; Nolan, A. M.; Liu, Y. S.; Gong, S.; Sun, Q.; Mo, Y. F. Lithium Chlorides and Bromides as Promising Solid-State Chemistries for Fast Ion Conductors with Good Electrochemical Stability. *Angew. Chem., Int. Ed.* **2019**, *58*, 8039.
- (20) Abdul Rashid, N. B.; Shan, Y. J.; Sugawara, K.; Tezuka, K. The effects of lattice volume and carrier concentration on the conductivity of NASICON-type  $\text{Li}_x\text{In}_{0.5}\text{Z}_{0.5}(\text{PO}_4)_3$  ( $\text{X} = \text{Ti}, \text{Zr}; \text{Z} = \text{Nb}, \text{Ta}$ ) oxides. *Ionics* **2021**, *27*, 3829.
- (21) Tanibata, N.; Takimoto, S.; Aizu, S.; Takeda, H.; Nakayama, M. Applying the HSAB design principle to the 3.5 V-class all-solid-state

- Li-ion batteries with a chloride electrolyte. *J. Mater. Chem. A* **2022**, *10*, 20756.
- (22) Wohlmuth, D.; Epp, V.; Bottke, P.; Hanzu, I.; Bitschnau, B.; Letofsky-Papst, I.; Kriechbaum, M.; Amenitsch, H.; Hofer, F.; Wilkening, M. Order vs. disorder—a huge increase in ionic conductivity of nanocrystalline LiAlO<sub>2</sub> embedded in an amorphous-like matrix of lithium aluminate. *J. Mater. Chem. A* **2014**, *2*, 20295.
- (23) Ikhwan, M.; Azis, R.; Hashim, M.; Holland, D.; Howes, A.; Zakaria, A.; Hassan, J. The Formation of Yttrium Aluminium Monoclinic ( $\text{Y}_4\text{Al}_2\text{O}_9$ ) by Sol-Gel Synthesis at Low Heating Temperature. *J. Aust. Ceram. Soc.* **2014**, *50*, 17.
- (24) Zettl, R.; Gombotz, M.; Clarkson, D.; Greenbaum, S. G.; Ngene, P.; de Jongh, P. E.; Wilkening, H. M. R. Li-Ion Diffusion in Nanoconfined LiBH<sub>4</sub>-LiI/Al<sub>2</sub>O<sub>3</sub>: From 2D Bulk Transport to 3D Long-Range Interfacial Dynamics. *ACS Appl. Mater. Interfaces* **2020**, *12*, 38570.
- (25) Düvel, A.; Romanova, E.; Sharifi, M.; Freude, D.; Wark, M.; Heitjans, P.; Wilkening, M. Mechanically Induced Phase Transformation of  $\gamma$ -Al<sub>2</sub>O<sub>3</sub> into  $\alpha$ -Al<sub>2</sub>O<sub>3</sub>. Access to Structurally Disordered  $\gamma$ -Al<sub>2</sub>O<sub>3</sub> with a Controllable Amount of Pentacoordinated Al Sites. *J. Phys. Chem. C* **2011**, *115*, 22770.
- (26) Walkley, B.; Provis, J. L. Solid-state nuclear magnetic resonance spectroscopy of cements. *Mater. Today Adv.* **2019**, *1*, 100007.
- (27) Kobera, L.; Brus, J.; Klein, P.; Dedecek, J.; Urbanova, M. Biaxial Q-shearing of <sup>27</sup>Al 3QMAS NMR spectra: Insight into the structural disorder of framework aluminosilicates. *Solid State Nucl. Magn. Reson.* **2014**, *57–58*, 29.
- (28) Breuer, S.; Pregartner, V.; Lunghammer, S.; Wilkening, H. M. R. Dispersed Solid Conductors: Fast Interfacial Li-Ion Dynamics in Nanostructured LiF and LiF: $\gamma$ -Al<sub>2</sub>O<sub>3</sub> Composites. *J. Phys. Chem. C* **2019**, *123*, 5222.
- (29) Dai, T.; Wu, S.; Lu, Y.; Yang, Y.; Liu, Y.; Chang, C.; Rong, X.; Xiao, R.; Zhao, J.; Liu, Y.; Wang, W.; Chen, L.; Hu, Y.-S. Inorganic glass electrolytes with polymer-like viscoelasticity. *Nat. Energy* **2023**, *8*, 1221.
- (30) Ardel, G.; Golodnitsky, D.; Peled, E.; Wang, Y.; Gang, W.; Bajue, S.; Greenbaum, S. Bulk and interfacial ionic conduction in LiI/Al<sub>2</sub>O<sub>3</sub> mixtures. *Solid State Ionics* **1998**, *113–115*, 477.
- (31) Zheng, J.; Tang, M.; Hu, Y.-Y. Lithium Ion Pathway within Li<sub>7</sub>La<sub>3</sub>Zr<sub>2</sub>O<sub>12</sub>-Polyethylene Oxide Composite Electrolytes. *Angew. Chem., Int. Ed.* **2016**, *55*, 12538.
- (32) Miyazaki, R.; Maekawa, H. Li<sup>+</sup>-Ion Conduction of Li<sub>3</sub>AlF<sub>6</sub> Mechanically Milled with LiCl. *ECS Electrochem. Lett.* **2012**, *1*, A87.
- (33) Thompson, T.; Yu, S.; Williams, L.; Schmidt, R. D.; Garcia-Mendez, R.; Wolfenstine, J.; Allen, J. L.; Kioupakis, E.; Siegel, D. J.; Sakamoto, J. Electrochemical Window of the Li-Ion Solid Electrolyte Li<sub>7</sub>La<sub>3</sub>Zr<sub>2</sub>O<sub>12</sub>. *ACS Energy Lett.* **2017**, *2*, 462.
- (34) Connell, J. G.; Fuchs, T.; Hartmann, H.; Krauskopf, T.; Zhu, Y.; Sann, J.; Garcia-Mendez, R.; Sakamoto, J.; Tepavcevic, S.; Janek, J. Kinetic versus Thermodynamic Stability of LLZO in Contact with Lithium Metal. *Chem. Mater.* **2020**, *32*, 10207.
- (35) Golozar, M.; Paoletta, A.; Demers, H.; Savoie, S.; Girard, G.; Delaporte, N.; Gauvin, R.; Guerfi, A.; Lorrmann, H.; Zaghib, K. Direct observation of lithium metal dendrites with ceramic solid electrolyte. *Sci. Rep.* **2020**, *10*, 18410.
- (36) Rosero-Navarro, N. C.; Miura, A.; Tadanaga, K. Composite cathode prepared by argyrodite precursor solution assisted by dispersant agents for bulk-type all-solid-state batteries. *J. Power Sources* **2018**, *396*, 33.
- (37) Kato, A.; Nose, M.; Yamamoto, M.; Sakuda, A.; Hayashi, A.; Tatsumisago, M. Mechanical properties of sulfide glasses in all-solid-state batteries. *J. Ceram. Soc. Jpn.* **2018**, *126*, 719.
- (38) Schwietert, T. K.; Arszelewska, V. A.; Wang, C.; Yu, C.; Vasileiadis, A.; de Klerk, N. J. J.; Hageman, J.; Hupfer, T.; Kerkamm, I.; Xu, Y.; van der Maas, E.; Kelder, E. M.; Ganapathy, S.; Wagelmaker, M. Clarifying the relationship between redox activity and electrochemical stability in solid electrolytes. *Nat. Mater.* **2020**, *19*, 428.
- (39) Ren, Y.; Sun, C. J.; Liu, J. J.; Cai, G. J.; Tan, X.; Zhang, C. Effect of the mechanical strength on the ion transport in a transition metal lithium halide electrolyte: first-principle calculations. *Mater. Today Commun.* **2022**, *33*, 104570.
- (40) Balaish, M.; Gonzalez-Rosillo, J. C.; Kim, K. J.; Zhu, Y.; Hood, Z. D.; Rupp, J. L. M. Processing thin but robust electrolytes for solid-state batteries. *Nat. Energy* **2021**, *6*, 227.
- (41) Sakuda, A.; Hayashi, A.; Tatsumisago, M. Sulfide Solid Electrolyte with Favorable Mechanical Property for All-Solid-State Lithium Battery. *Sci. Rep.* **2013**, *3*, 2261.
- (42) Fyfe, W. S. *Geochemistry*; Oxford University Press, 1974.
- (43) Finsterbusch, M.; Danner, T.; Tsai, C.-L.; Uhlenbruck, S.; Latz, A.; Guillou, O. High Capacity Garnet-Based All-Solid-State Lithium Batteries: Fabrication and 3D-Microstructure Resolved Modeling. *ACS Appl. Mater. Interfaces* **2018**, *10*, 22329.
- (44) Yu, R.; Wang, C.; Duan, H.; Jiang, M.; Zhang, A.; Fraser, A.; Zuo, J.; Wu, Y.; Sun, Y.; Zhao, Y.; Liang, J.; Fu, J.; Deng, S.; Ren, Z.; Li, G.; Huang, H.; Li, R.; Chen, N.; Wang, J.; Li, X.; Singh, C. V.; Sun, X. Manipulating Charge-Transfer Kinetics of Lithium-Rich Layered Oxide Cathodes in Halide All-Solid-State Batteries. *Adv. Mater.* **2023**, *35*, 2207234.
- (45) Koerver, R.; Aygün, I.; Leichtweiß, T.; Dietrich, C.; Zhang, W.; Binder, J. O.; Hartmann, P.; Zeier, W. G.; Janek, J. Capacity Fade in Solid-State Batteries: Interphase Formation and Chemomechanical Processes in Nickel-Rich Layered Oxide Cathodes and Lithium Thiophosphate Solid Electrolytes. *Chem. Mater.* **2017**, *29*, 5574.
- (46) Wu, Y.; Zhou, K.; Ren, F.; Ha, Y.; Liang, Z.; Zheng, X.; Wang, Z.; Yang, W.; Zhang, M.; Luo, M.; Battaglia, C.; Yang, W.; Zhu, L.; Gong, Z.; Yang, Y. Highly reversible Li<sub>2</sub>RuO<sub>3</sub> cathodes in sulfide-based all solid-state lithium batteries. *Energy Environ. Sci.* **2022**, *15*, 3470.
- (47) Zhou, L.; Zuo, T.-T.; Kwok, C. Y.; Kim, S. Y.; Assoud, A.; Zhang, Q.; Janek, J.; Nazar, L. F. High areal capacity, long cycle life 4 V ceramic all-solid-state Li-ion batteries enabled by chloride solid electrolytes. *Nat. Energy* **2022**, *7*, 83.
- (48) Sun, S.; Zhao, C.-Z.; Yuan, H.; Fu, Z.-H.; Chen, X.; Lu, Y.; Li, Y.-F.; Hu, J.-K.; Dong, J.; Huang, J.-Q.; Ouyang, M.; Zhang, Q. Eliminating interfacial O-involving degradation in Li-rich Mn-based cathodes for all-solid-state lithium batteries. *Sci. Adv.* **2022**, *8*, No. eadd5189.
- (49) Miyazaki, R.; Hiroi, S.; Miyazaki, H.; Hihara, T. Improvement of Li<sup>+</sup> conductivity in ball-milled LiI and the local structure analysis by pair distribution function based on X-ray total scattering. *J. Solid State Electrochem.* **2022**, *26*, 1577.